



## **Final Draft of the original manuscript**

Andre, N.M.; Bouali, A.; Maawad, E.; Staron, P.; dos Santos, J.F.;  
Zheludkevich, M.L.; Amancio-Filho, S.T.:

**Corrosion behavior of metal–composite hybrid joints:  
Influence of precipitation state and bonding zones.**

In: Corrosion Science. Vol. 158 (2019) 108075.

First published online by Elsevier: 09.07.2019

<https://dx.doi.org/10.1016/j.corsci.2019.07.002>

“Corrosion behavior of metal–composite hybrid joints: Influence of precipitation state and bonding zones”

Natalia M. André<sup>1\*</sup>, Anissa Bouali<sup>2</sup>, Emad Maawad<sup>3</sup>, Peter Staron<sup>3</sup>, Jorge F. dos Santos<sup>1</sup>, Mikhail L. Zheludkevich<sup>2,5</sup>, Sergio T. Amancio-Filho<sup>4</sup>

<sup>1</sup> Helmholtz-Zentrum Geesthacht, Centre for Materials and Coastal Research, Institute of Materials Research, Materials Mechanics, Solid State Joining Processes, Geesthacht, Germany

<sup>2</sup> Helmholtz-Zentrum Geesthacht, Centre for Materials and Coastal Research, Magnesium Innovation Center, Corrosion and Surface Technology, Geesthacht, Germany

<sup>3</sup> Helmholtz-Zentrum Geesthacht, Institute of Materials Research, Geesthacht, Germany

<sup>4</sup> Graz University of Technology – TU Graz, Institute of Materials Science, Joining and Forming, BMVIT Endowed Professorship for Aviation, Kopernikusgasse 24/1, 8010 Graz – Austria

<sup>5</sup> Faculty of Engineering, University of Kiel, Kaiserstrasse 2, 24143 Kiel, Germany

\*Corresponding author: Tel./Fax: +49 4152 87-2032/ 2033 email: [natalia.manente@hzg.de](mailto:natalia.manente@hzg.de)

## Abstract

The corrosion behavior of AA2024-T3/carbon-fiber-reinforced polyphenylene sulfide joints was investigated. The joints were exposed to salt spray from one to six weeks. The residual strength of these joints was assessed using lap shear test. The corroded surfaces and interfaces were analyzed using small angle X-ray scattering, scanning electron microscopy, and energy dispersive spectroscopy. Regarding the top surface of the joints, the aluminum part corroded preferably in the heat-affected zone (HAZ). It was demonstrated that the HAZ is more susceptible to corrosion than the stir zone (SZ) due to the anodic sites formed by coarse intermetallic particles and S'(S) phase precipitation. Besides, the macro-galvanic coupling between the zones may also potentialize the corrosion in HAZ as the base material and SZ displayed a lower volume fraction of S'(S) than HAZ. In addition, the corrosion at the interface of the joints was evaluated. Four different stages in the development of corrosion at the interface were identified. At Stage I, the joints showed fast strength degradation (0% to -24% of ultimate lap shear force (ULSF)) due to water absorption and NaCl migration into the composite. At Stage II, the strength degradation of the joints was stalled (-24% to -28% of ULSF) due to the protection provided to the bonding area by the reconsolidated layer of polymer at the borders of the joint. The polymeric layer acted

as a protective coating on the aluminum surface. At Stage III, the corrosion overcame the polymeric layer by reaching the bonding area of the joint. As a result, the strength of the joints rapidly degraded from -28% to -44% of ULSF. Finally, at Stage IV, one expects generalized corrosion in the bonding area, leading to the final strength degradation of the joint.

**Keywords:** Hybrid structure, composite, pitting, intergranular corrosion, galvanic corrosion, residual strength

## 1. Introduction

The use of metal–composite hybrid structures proved to be an advantageous alternative to reduce weight and fuel consumption of cars and aircrafts [1,2]. Owing to the high specific strength and stiffness of composite materials, robust structures can be constructed by their combination with lightweight metal alloys. Most famous examples of use are the A350 XWB [1] and the Boeing 787 [3], along with the new generation of fully electric and hybrid cars of BMW (e.g. i3 and i8) [4].

Nevertheless, the cost-effectiveness of combining these hybrid materials relies also on the challenges of joining them due to the high dissimilarity of their properties [5]. Currently, mechanical fastening and adhesive bonding are the most common techniques for joining hybrid structures in mass production [6]. However, limitations like stress concentration and weight penalty (for rivets or bolts) are often related to mechanical fastening, whereas extensive surface preparation and long curing time come along with adhesive bonding [5]. Therefore, a number of joining technologies have been developed, focusing on mitigating such drawbacks [7–10].

Friction Spot Joining (FSpJ) is an alternative technology for joining metal–composite structures [11]. This technology uses a non-consumable tool to generate frictional heat and plastically deform the metallic component of the joint into the composite [12]. Three main bonding zones are found in friction spot joints: the plastically deformed zone (PDZ), the transition zone (TZ), and the adhesion zone (AZ) [13]. PDZ comprises the central region of the bonding area. In this zone, the main bonding mechanisms are macro- and micro-mechanical interlocking. Macro-mechanical interlocking results from the metal deformation into the composite, while micro-mechanical interlocking results from polymer and fiber entrapment on the aluminum surface [13]. AZ is the outer region of the bonding area. The softened/molten polymer displaced from the center of the joint during the joining process accumulates in

this region [13]. The main bonding mechanism in AZ is the adhesive forces provided by the reconsolidation of the molten polymeric material [13]. TZ, as the name implies, is the transition zone between PDZ and AZ. This zone is characterized by the presence of air bubbles as a result of the outflow of molten polymer during the joining process [13].

Several combinations of materials have been successfully joined using FSpJ. Goushegir *et al.* [14] achieved shear strengths of 38–123 MPa for AA2024-T3 and carbon-fiber-reinforced polyphenylene sulfide (CF-PPS) joints. Other combinations of materials, such as AA2024-T3/PPS/CF-PPS shown by André *et al.* [15], AA6181-T4/CF-PPS shown by Esteves *et al.* [16], and AZ31-O/CF-PPS shown by Amancio *et al.* [12], were successfully investigated in recent years. Despite the success in producing friction spot joints with high mechanical performance in previous investigations, the galvanic corrosion behavior of such joints has not yet been addressed.

The chemical composition and temperature of an environment can significantly deteriorate the joint mechanical performance through corrosion [17]. Airplanes and cars are designed to survive diverse environments worldwide, including marine and other corrosive atmospheres [18,19]. These structures are also often in contact with the maintenance chemicals during their respective service lives, which can lead to corrosion [18,19]. Additionally, the galvanic coupling of metal alloys and carbon fibers is a well-known issue for metal–composite connections [5,20]. The carbon fibers are electrochemical noble materials, i.e., they usually present relatively high potentials [21]. In contrast, metallic alloys typically present more negative potential [21]. Therefore, when coupled, a significant potential difference between metals and fiber reinforcements of composites is generated: the ASTM G82-98 galvanic series reports values up to -1.0 V for aluminum alloys and +0.2 V for pure graphite [25]. The potential difference between the materials acts as the driving force for the onset/acceleration of the corrosion phenomenon in the metallic component [21].

One of the reasons for the enhanced corrosion susceptibility of metal alloys is related to the diverse types of particles and inclusions distributed over the grains and their boundaries, which are formed during the processing of the alloys [22,23]. Precipitates and intermetallic particles can act as local cathodes raising the corrosion susceptibility of the adjacent areas or anodes undergoing accelerated dissolution [24].

Fiore *et al.* [26] investigated the corrosion under salt spray of AA6060-T6/CF-epoxy riveted joints. The authors showed decreases of up to 46% in strength after 15 weeks of exposure due to deterioration of the mechanical properties of the composite. The influence of galvanic corrosion on the strength degradation of the joints was minimum in that study. In another work, Pan *et al.* [27] demonstrated the occurrence of galvanic corrosion as a degradation mechanism of magnesium alloys (LZ91, LZ141, and AZ31) in contact with CFRP. Similar behavior was observed by Belucci *et al.* [21] for aluminum alloys (AA2024-T3 and AA7075-T6) connected with graphite-epoxy.

In the current study, the corrosion behavior of AA2024-T3/CF-PPS friction spot joints was investigated using salt spray test. First, the influence of the joining process on the microstructure and precipitation state of the aluminum alloy was assessed using optical microscopy and small angle X-ray scattering (SAXS). Thus, the corrosion evolution on the top surface of the joints was described in accordance with the microstructural zones formed due to the FSpJ process. In addition, the corrosion at the interface of the joints was evaluated. Scanning electron microscopy (SEM) and energy dispersive spectroscopy (EDS) were used to identify the different stages of corrosion development at the interface. The role of each bonding zone of the joint was elucidated within the corrosion degradation process at the interface of the joined materials. Finally, the global strength degradation of the joints was correlated with the corrosion damage in the bonding zones.

## **2. Materials and Methods**

### **2.1. Aluminum alloy 2024-T3**

The aluminum alloy 2024-T3 was selected as the metallic part to produce the joints in the investigation. This is a precipitation hardenable alloy with Cu and Mg as the principal alloying elements. The addition of copper and magnesium provides high strength to the alloy through pinning of dislocations. Copper acts through solid solution strengthening, while Mg creates precipitates by natural aging [28]. Cu-rich intermetallic particles are also formed during the alloy processing. Figure 1 shows the microstructure of the aluminum alloy used in this work. The intermetallic particles are observed to be distributed in the grains and their boundaries. The precipitates and intermetallic particles act as cathodes, raising the intergranular and exfoliation corrosion susceptibility of the adjacent areas in the alloy [24].

Therefore, the corrosion resistance of the AA2024-T3 is generally not as good as other aluminum alloy series (e. g. the 6XXX series) [24].

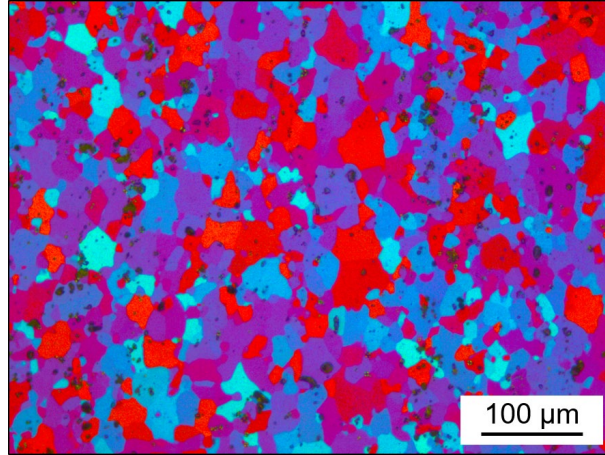


Figure 1: Microstructure of AA2024-T3 transverse to the rolling direction.

The AA2024-T3 is widely used in the aircraft industry due to its high strength and excellent fatigue performance [23]. 2 mm-thick rolled sheets, provided by Constellium (France), were used in this work. Table 1 presents the nominal chemical composition of the alloy. Table 2 lists selected physical and mechanical properties of this alloy [29].

Table 1: Nominal chemical composition of AA2024-T3.

Element	Cu	Mg	Mn	Fe	Zn	Si	Ti	Cr	Al
Wt%	4.55	1.49	0.45	0.17	0.16	0.10	0.02	<0.01	Bal.

Table 2: Selected physical and mechanical properties of AA2024-T3 [29].

Tensile Strength (TL direction) [MPa]	Yield Strength (TL direction) [MPa]	Elongation [%]	Incipient Melting Temperature [°C]	Thermal Conductivity [W m <sup>-1</sup> K <sup>-1</sup> ]	Coefficient of Thermal Expansion, 20–300°C [μm m <sup>-1</sup> °C <sup>-1</sup> ]
437	299	21	502	121	24.7

## 2.2. Carbon-fiber-reinforced polyphenylene sulfide (CF-PPS)

Carbon-fiber-reinforced polyphenylene sulfide (CF-PPS) was selected as the composite part to produce the joints in this work. CF-PPS retains an outstanding performance at high temperatures and is used for several applications in aerostructures [30]. Exemplary applications are the “J-Nose” sub-frame

wings of Airbus A380 and the engine pylon cover of Airbus A340-500/600 [30]. This quasi-isotropic laminate composite consists of seven carbon-fiber-fabric reinforcement plies in the  $[(0.90)/(\pm 45)]_3/(0.90)$  sequence. In this work, a 2.17 mm-thick laminate with 43 wt% carbon fibers, produced by Tencate (Netherlands), was used. Table 3 presents a selection of physical and mechanical properties of the CF-PPS.

Table 3: Selected physical and mechanical properties of the CF-PPS [30].

Tensile Strength (warp/weft) [MPa]	In-Plane Shear Strength [MPa]	Glass Transition Temperature [°C]	Melting Temperature [°C]	Thermal Conductivity [ $\text{W m}^{-1} \text{K}^{-1}$ ]	Coefficient of Thermal Expansion, 23–300°C [ $\mu\text{m m}^{-1} \text{°C}^{-1}$ ]
790/750	119	120	280	0.19	52.2

## 2.3. Experimental Procedure

### 2.3.1. Production of the joints

Sandblasting was used on the aluminum alloy before the joining process to increase its surface roughness and adhesion to the composite [14,31]. Alumina corundum was used as the medium ( $\text{Al}_2\text{O}_3$ , average particle size: 100–150  $\mu\text{m}$ ). Sandblasting was performed for 10 s from a distance of 20 cm and an incidence angle of  $45^\circ$  between the blasting pistol and the aluminum part. The average surface roughness ( $R_a$ ) obtained was  $6.7 \pm 0.4 \mu\text{m}$ .

The joints were produced in a single overlap configuration (Figure 2) to allow their mechanical testing after the exposure to salt spray. The joining equipment RPS 200 (Harms & Wende, Germany) was employed in this study. A non-consumable tool made of molybdenum-vanadium hot-work tool steel was used (Figure 3-A). The sleeve-plunge variant of FSpJ was employed to produce the joints in this study. Figure 3-B presents the steps of the FSpJ process: (a) positioning of the parts and the tool, (b) plunging of the sleeve and plasticization of the metal part, (c) refilling of the keyhole formed by the sleeve plunging, and (d) consolidation of the joint under pressure. For details about the FSpJ process, please refer to [12]. The joints were produced using the following joining parameters: 2900 rpm of rotational speed, 0.8 mm of plunge depth, 8 s of joining time, and 6 kN of joining force. This combination of joining parameters was obtained from a previous statistical optimization (design of experiments combined with analysis of variance) to maximize the lap shear strength of the joints. The optimization study is beyond the scope of this work and therefore will be published elsewhere.

The process temperature evolution was monitored with an infrared thermo-camera (Infratec, Germany) set within the range of 150–700°C. The data acquisition frequency was 80 Hz. The measurements were performed on the aluminum surface close to the tool.

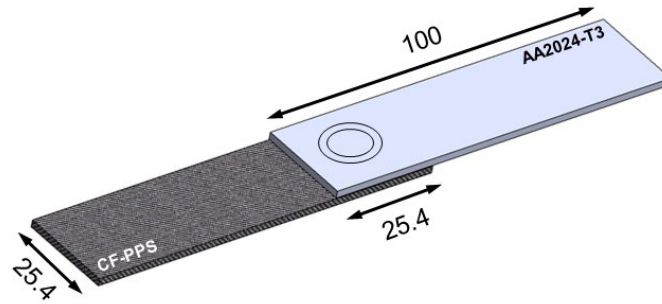


Figure 2: Configuration and dimensions of the joints (in mm).

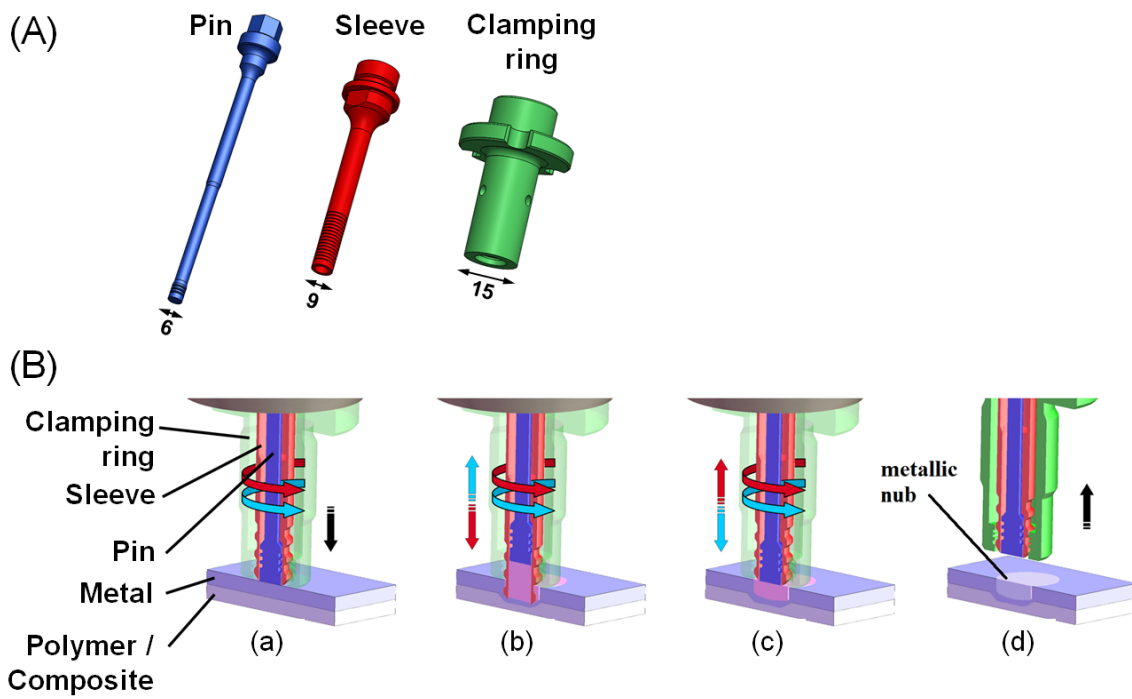


Figure 3: (A) Tool used in this work (dimensions in mm). (B) Steps of the FSpJ process: (a) positioning of parts and tool, (b) plunging of the sleeve and plasticization of the metal, (c) refilling of the keyhole, and (d) joint consolidation (Adapted from [32]).

### 2.3.2. Microstructural analysis

The microstructural changes caused by the joining process were assessed using optical microscopy. The top surface of the spot joint was polished and etched (Barker, 25 V, 90 s) to reveal the microstructure of the aluminum after the joining process.

Small angle X-ray scattering (SAXS) was performed along a longitudinal line crossing the center of the joint to investigate the size and volume fraction of the precipitates in the different microstructural zones of the joint, as indicated in Figure 4. The scan line was 50 mm long, with a step size of 1 mm between the measured points. The measurements were performed using X-rays with an energy of 87.1 keV. The beam had a cross-section of 0.2 mm × 0.2 mm, the distance between the sample and the detector was 3460 mm, and a beam stop with a diameter of 1 mm was used. A Perkin-Elmer area detector with a pixel size of 200 μm and an exposure time of 20 s was used. An empty measurement without sample, corrected for the sample transmission, was subtracted from each image. The images were reduced to scattering curves through azimuthal integration using the program Fit2d [33]. Scattering curves were analyzed based on the two-phase model of particles in a homogeneous matrix. All the precipitates were modeled as spheres. Two lognormal size distributions were used to fit the measured scattering curves using a least squares algorithm. Interparticle interference was taken into account using the local monodisperse approximation [34]. A constant isotropic contribution was added to the scattering of the precipitates.

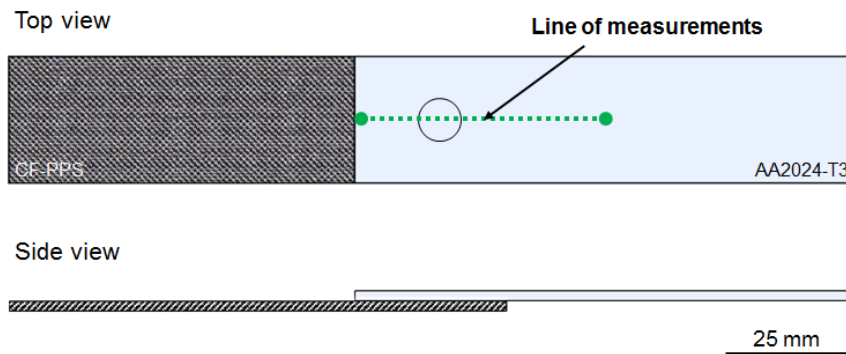


Figure 4: Schematic drawing showing the SAXS measurements on the aluminum surface of the joint.

### 2.3.3. Local mechanical performance

Microhardness measurements were performed at the top surface of a friction spot joint to evaluate the influence of FSpJ on the local mechanical performance of the aluminum alloy. The indents

were performed on half of the overlap area of the joint (25 mm x 12.5 mm), considering its symmetry. The indentation force was 200 g and the distance between indents was 0.3 mm in agreement with the ASTM E384-10 standard procedure.

#### **2.3.4. Electrochemical characterization**

The materials used to produce the joints were electrochemically characterized using potentiodynamic polarization. It is important to note that the electrochemical properties of the CF-PPS varies according to the amount of exposed carbon fibers on its surface. Therefore, the measurements for the CF-PPS were performed using a sample extracted from the PDZ of the joints to ensure a maximum fiber exposition. For the AA2024-T3, a standard sandblasted surface was used.

The electrochemical measurements were performed using an Interface 1000E Potentiostat/galvanostat/ZRA (Gamry) embedded with a Gamry framework system. The potentiodynamic polarization of AA2024-T3 and CF-PPS was conducted in a three-electrode system. The test sample was the working electrode, while platinum and silver/silver chloride (Ag/AgCl) were the counter and reference electrodes respectively. A scan rate of 1 mV/s was employed and the measurements started after 6 minutes immersion in  $E_{oc}$  conditions. The potentiodynamic polarization for AA2024-T3 samples was run from -0.2 V to 1V vs. stable  $E_{oc}$  (~-0,58V) and following the anodic direction, whereas for CF-PPS the scan was over the 0.2 V to -1 V range vs. stable  $E_{oc}$  (~-0.08V) and following the cathodic direction. The experiments were repeated at least three times. The measurements were performed at room temperature in a solution of 0.5 % NaCl.

#### **2.3.5. Salt spray test**

The hybrid joints were placed vertically at an angle of 30° in a salt spray chamber for one, two, three, four, five, and six weeks. In accordance with ASTM B117-16, the chamber was kept at 35°C with the pressure of 1 bar and concentration of 5% NaCl of the salty fog. Five replicates were tested for each exposure time.

#### **2.3.6. Global mechanical performance**

The residual strength of the joints after exposure was evaluated using lap shear testing. The tests were performed using a universal testing machine Zwick/Roell 1478 with a cross-head speed of 1.27 mm min<sup>-1</sup> at room temperature. Specimens with dimensions of 100 x 45 mm (2025 mm<sup>2</sup> overlap area) were tested, as depicted in Figure 2. The average residual shear strength of the joints was evaluated based on five replicates.

### 2.3.7. Corroded surface analysis

The top surface and the fracture surface of the joints were analyzed after the salt spray exposure using scanning electron microscopy (SEM) and energy dispersive spectroscopy (EDS). Prior to the examination, the surfaces were sputtered with gold. The images were taken using a voltage of 10 kV and at a working distance of approximately 10 mm.

## 3. Results and Discussion

### 3.1. Corrosion development on the top surface of the joints

#### 3.1.1. Process-related changes on microstructure and precipitation state of the aluminum part

Figure 5 presents the typical temperature evolution during the FSpJ process. During the FSpJ process, the maximum temperature achieved was  $375 \pm 15$  °C on the aluminum surface, which corresponds to 75% of the incipient melting temperature of AA2024-T3 (502 °C). The combination of such high temperatures and shear rates applied by the tool resulted in changes of the microstructure and the precipitation state of the AA2024-T3.

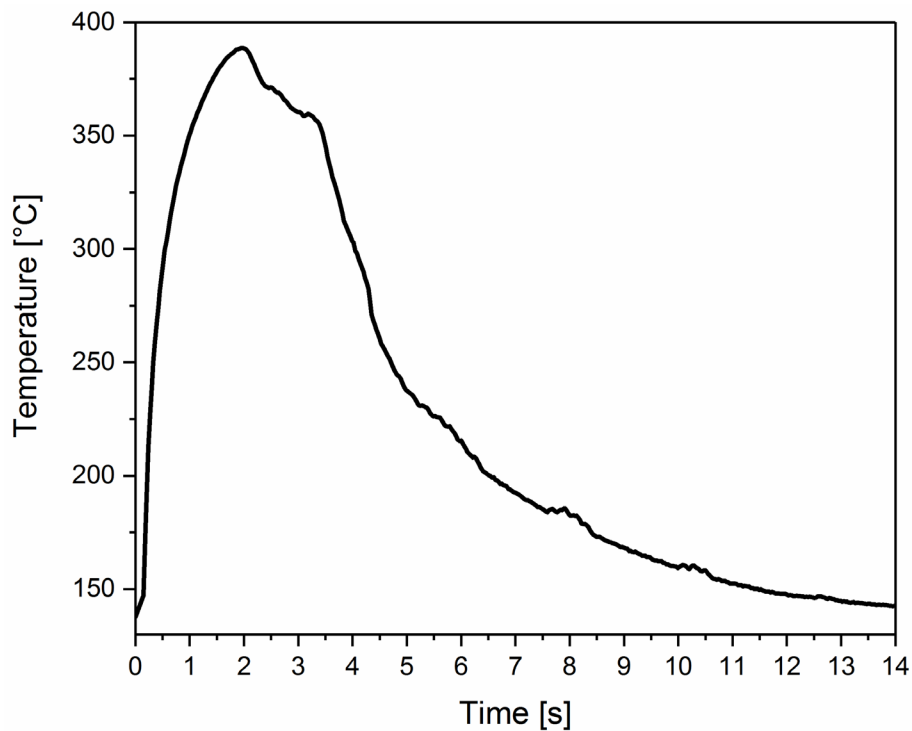


Figure 5: Representative example of the temperature evolution on the aluminum surface during FSpJ for the joining parameters used in this study.

As previously reported [14], FSpJ generates three different microstructural zones in the metallic part of the joints: stir zone (SZ), thermo-mechanically affected zone (TMAZ), and heat-affected zone (HAZ), as indicated in Figure 6-A. In this study, the corrosion behavior of the joint is the main concern. Hence, the surface of the joint is the region of interest. Considering the top surface of the joint, the TMAZ corresponds to a limited area between SZ and HAZ. Therefore, only the latter two will be analyzed in details in this section.

The combination of high temperatures ( $375\text{ }^{\circ}\text{C} > 0.6T_m$  of AA2024-T3) and high shear rates imposed by the rotating sleeve lead to the dynamic recrystallization of the AA2024-T3 in the SZ. Therefore, fine grains are observed in this zone (Figure 6-C). One may also note that the coarse intermetallic particles present in the base material (BM) were stirred and refined in the SZ (Figure 6-C). In addition, the precipitation state of the alloy changes above  $300\text{ }^{\circ}\text{C}$ . The GPB zones are dissolved and the S'(S) metastable phase is precipitated [35]. Nevertheless, as the process temperature increases further ( $375\text{ }^{\circ}\text{C}$ ), the partial dissolution of S'(S) can increase the Cu content in the matrix and lead to a re-precipitation of GPB zones during cooling or at room temperature [35]. As a result, the fraction of GPB and S'(S) phases are similar between SZ and BM (Figure 7). The combination of grain refinement and precipitation sequence also results in similar hardness for SZ and BM (ca. 150 HV, Figure 8).

In contrast, no visible changes are observed in the microstructure in the HAZ. The shape and size of the grains, as well as the presence of coarse intermetallic particles, are identical to the BM (Figure 6-D). Nevertheless, the hardness of the HAZ is lower than that of the BM (ca. 128 HV, Figure 8). This decrease in hardness is caused by the dissolution of fine GPB zones above  $300\text{ }^{\circ}\text{C}$  due to the FSpJ process. Figure 7 demonstrates a decrease of approximately 30% in the volume fraction of GPB zones in the HAZ in comparison with BM and SZ. One also observes that the volume of coarse S'(S) precipitates is strongly increased in the HAZ when compared to BM and SZ; an increase of approximately 700% (Figure 7). This demonstrates that the temperature history in the HAZ during the FSpJ process was such that a significant volume fraction of S'(S) precipitated after the GPB zones dissolution. Nevertheless, the re-precipitation of GPB zones was not complete. This is consistent with other observations of the non-isothermal precipitation kinetics of this alloy in other friction-based joining processes [35,36].

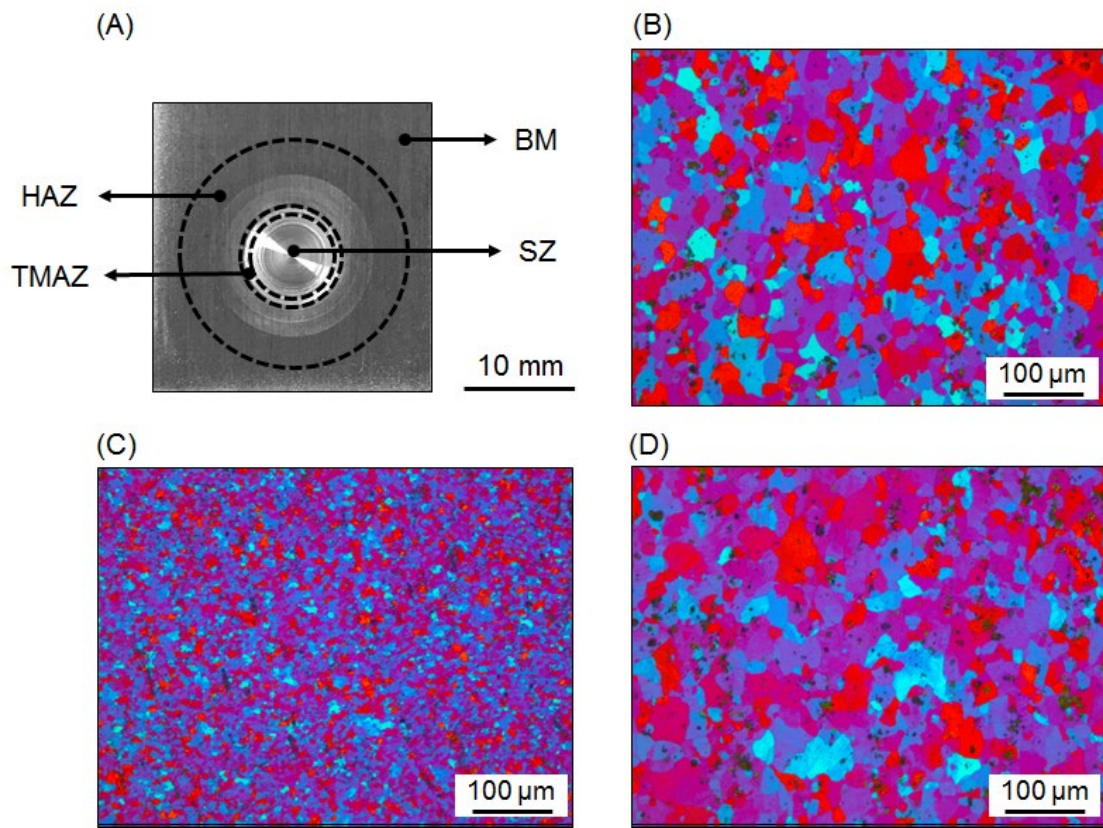


Figure 6: (A) Typical top surface of friction spot joints showing the delimitations for the microstructural zones. Microstructural details of (B) base material, (C) SZ, (D) HAZ.

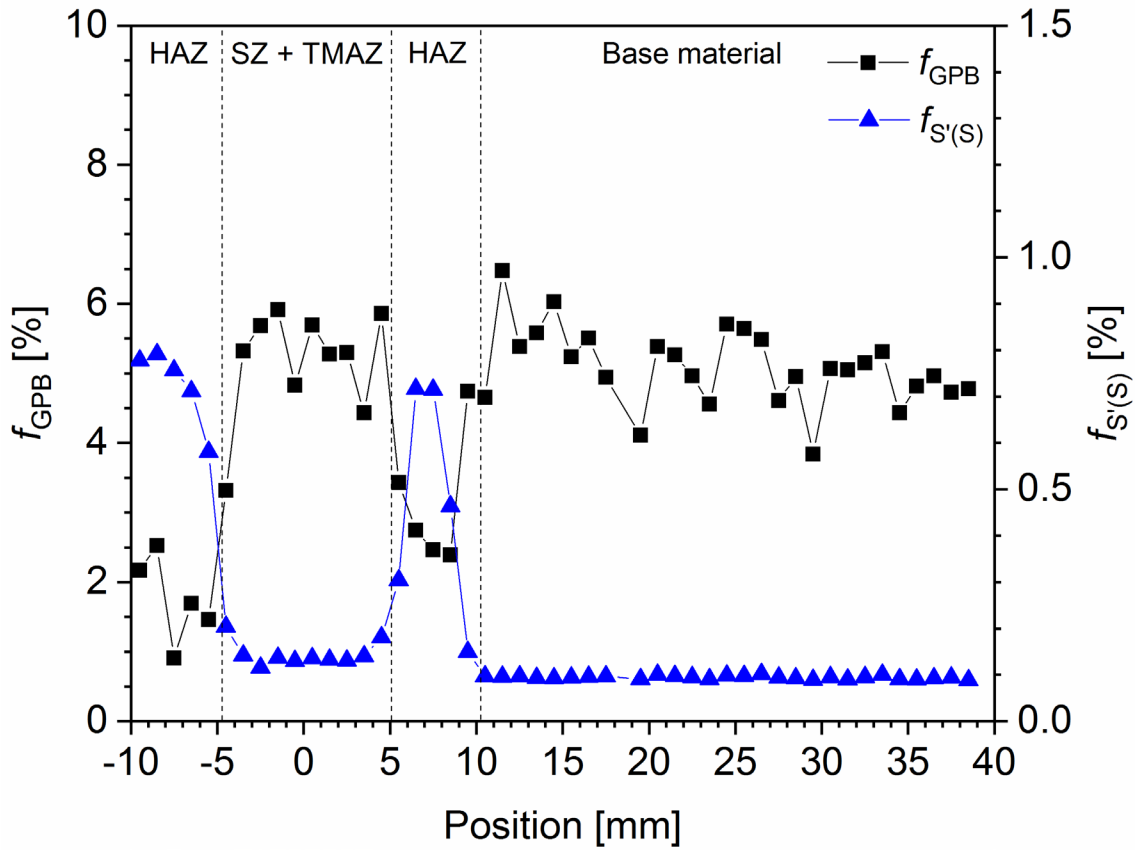


Figure 7: Volume fraction of GPB and S'(S) precipitates along a line across the friction spot joint determined by SAXS.

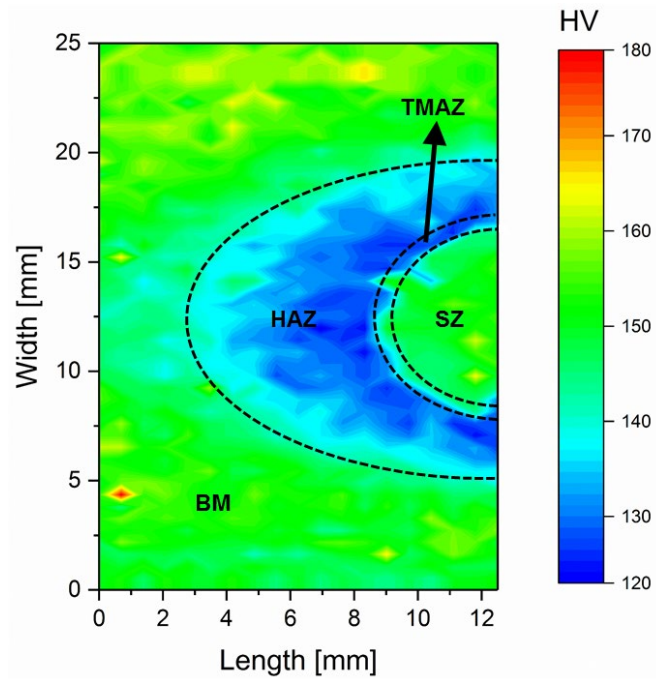


Figure 8: Typical microhardness profile of the top surface of friction spot joints.

### 3.1.2. Corrosion evolution at the top of the spot joint: Influence of the FSpJ process

Figure 9 presents the corrosion evolution on the top surface of the spot joint. It is possible to notice that the corrosion process starts heterogeneously through the formation of pits (Figure 9-B). Figure 10-A shows two developed pits on the aluminum surface after one week of exposure. As the time of exposure increases, the pits become deeper and start to connect themselves through a network of intergranular corrosion paths (Figure 10-B). Thus, the corrosion evolves beneath the surface and causes superficial exfoliation (black arrows in Figures 9-B to G). An overview of the exfoliation on the surface after six weeks of exposure is given in Figure 10-D. This corrosion process has been reported in the literature for AA2024-T3 [28–30], including its welds produced by other friction-based processes [40,41].

Additionally, one observes that the corrosion process does not evolve homogeneously on the top surface of the joint. This is a result of the different microstructural zones created during the thermo-mechanical cycle imposed by the joining process. Figure 9 demonstrates that the corrosion evolves rapidly at the HAZ, while the coupled region comprising TMAZ and SZ is barely attacked after six weeks of exposure.

As discussed earlier, GPB zones are the predominant precipitates in the SZ, as indicated in Figure 7. The GPB zones comprise fine precipitates, which are often distributed in the matrix of the alloy instead of the grain boundaries [35]. During their precipitation, these zones decrease the Cu content in the matrix and thereby reduce the matrix breakdown potential [42]. The lower content of Cu in the matrix also decreases the differential potential between matrix and Cu-depletion zones formed around the grain boundaries due to S'(S) precipitation [42]. Therefore, both pitting and intergranular attacks are not prone in this zone.

In contrast, the HAZ presented coarse intermetallic particles and a high volume of S'(S) phase in its microstructure (Figures 6 and 7). Coarse intermetallic particles and the S'(S) phase precipitation create active sites, which are prone to self-corrosion in the beginning and rapidly converted to active local Cu-rich cathodes as a result of dealloying [43]. Therefore, the corrosion susceptibility of the HAZ is increased in comparison with the SZ [44]. The S'(S) precipitates are often associated with the formation of precipitate-free and Cu-depletion zones around the grain boundaries during their formation [44]. These zones create a potential gradient at the region around the grain boundaries, consequently increasing the susceptibility of intergranular corrosion [44]. Besides, macro-galvanic coupling may also potentialize the

corrosion in the HAZ. BM and SZ display a similar profile of particles, presenting a lower volume fraction of S'(S) than HAZ (Figure 7). Therefore, one expects that a macro-difference of potentials is established when BM and SZ are coupled with the HAZ in a corrosive environment.

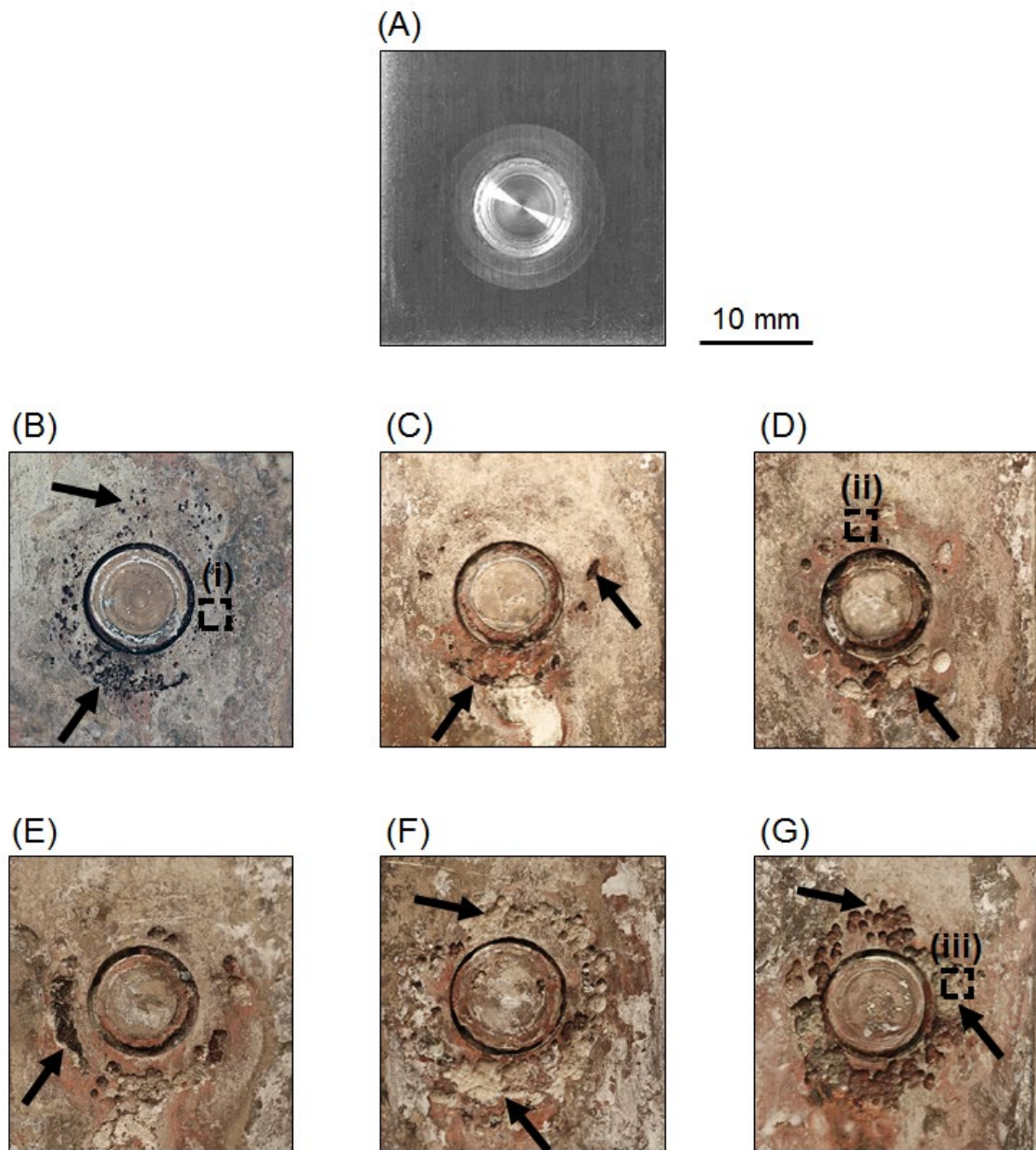


Figure 9: Top surface of the spot joint (A) as joined and after (B) one week, (C) two weeks, (D) three weeks, (E) four weeks, (F) five weeks, and (G) six weeks of exposure.

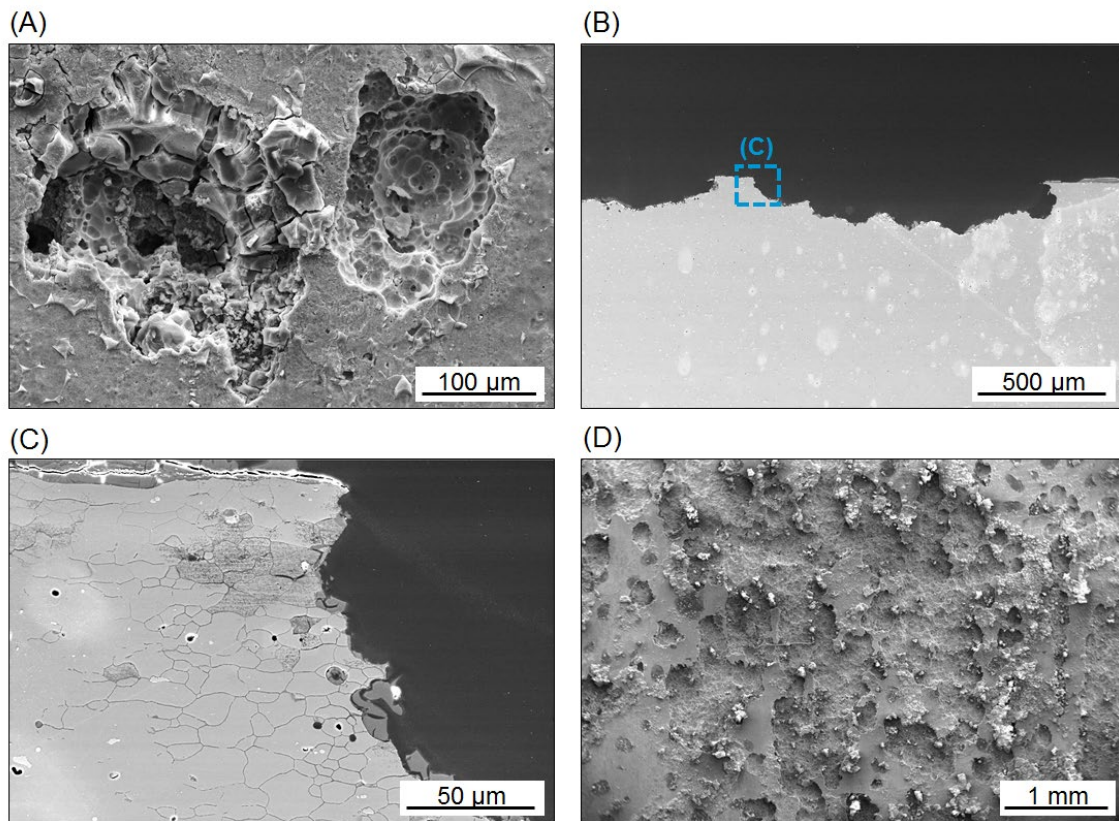


Figure 10: (A) Pits developed at the aluminum surface after one week of exposure (Region i from Figure 9-B). (B) Cross-sectional view of the connection between two pits after three weeks of exposure (Region ii from Figure 9-D). (C) Detail from (B) showing intergranular corrosion of the aluminum part. (D) Overview of exfoliation at the aluminum surface because of pitting and intergranular corrosion after six weeks of exposure (Region iii from Figure 9-G).

### 3.2. Corrosion development at the interface of friction spot joints

#### 3.2.1. Electrochemical characterization of the AA2024-T3/CF-PPS couple

The obtained potentiodynamic curves for both CF-PPS and AA2024-T3 are represented in Figure 11-A. The scan window was reduced to focus mostly on the cathodic branch related to CF-PPS and the anodic branch of AA2024-T3. Using the Tafel fitting procedure provided by the Gamry Echem software, the  $E_{\text{corr}}$  was estimated to be close to 0.15 V for CF-PPS and -0.57 V for AA2024-T3. This result is expected and in accordance with the ASTM G82-98 galvanic series, which reports values from -0.4 to -1.0 V for aluminum alloys and +0.2 V for pure graphite [25]. These observations demonstrate the anodic activity of the aluminum compared to that of the composite. Therefore, one expects that, when

electrically connected, the aluminum part of the joints would corrode while the composite part serves as a cathode.

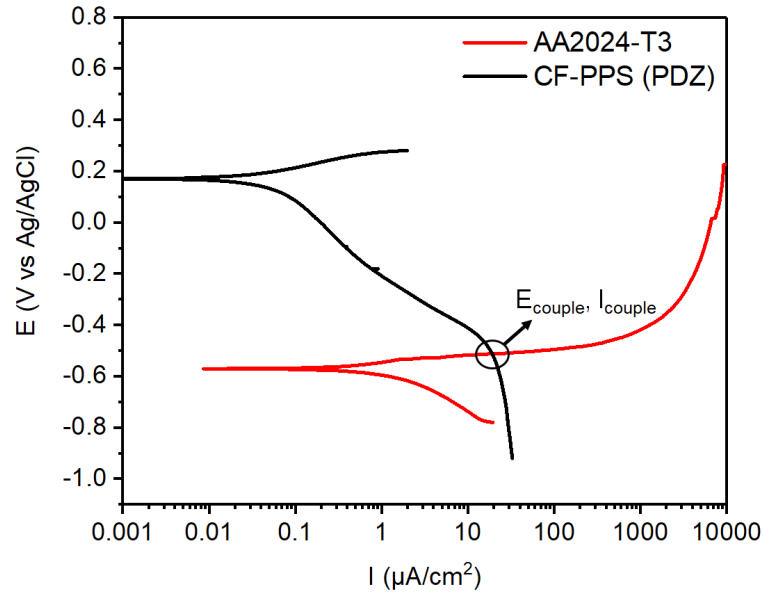


Figure 11: Potentiodynamic polarization curves of AA2024-T3 and CF-PPS.

Additionally, according to the mixed potential theory [25], the intersection between the cathodic polarization curve of the CF-PPS and the anodic polarization curve of the AA2024-T3 allows the deduction of the potential and current of the galvanic couple AA2024-T3/CF-PPS used in this work. Such properties were found to be  $E_{\text{couple}} = -0.52 \text{ V}$  and  $I_{\text{couple}} = 19 \mu\text{A}/\text{cm}^2$  (Figure 11). Pan *et al.* [27] reported  $I_{\text{couple}} = 56 \mu\text{A}/\text{cm}^2$  for the AZ31/CF-epoxy couple. In another study, Mandel *et al.* [19] investigated the corrosion behavior of self-pierced hybrid joints. In that case, the authors measured an  $I_{\text{couple}} = 170 \mu\text{A}/\text{cm}^2$  for AA6060-T6/CF-epoxy. In both studies, the measured corrosion currents were significantly higher than those measured for the couple AA2024-T3/CF-PPS in this work. It indicates a higher galvanic corrosion resistance of AA2024-T3/CF-PPS compared to AZ31/CF-epoxy [27] and AA6060-T6/CF-epoxy [19].

### 3.2.2. Corrosion evolution at the interface of the friction spot joint: The role of the bonding zones

Figure 12 shows the residual strength, while Figure 13 presents the fracture surfaces of the joints after the salt spray exposure. One observes that strength degradation occurred at different paces during the six weeks of exposure to the salt spray. The development of the corrosion on the interface of the joints was divided into four stages.

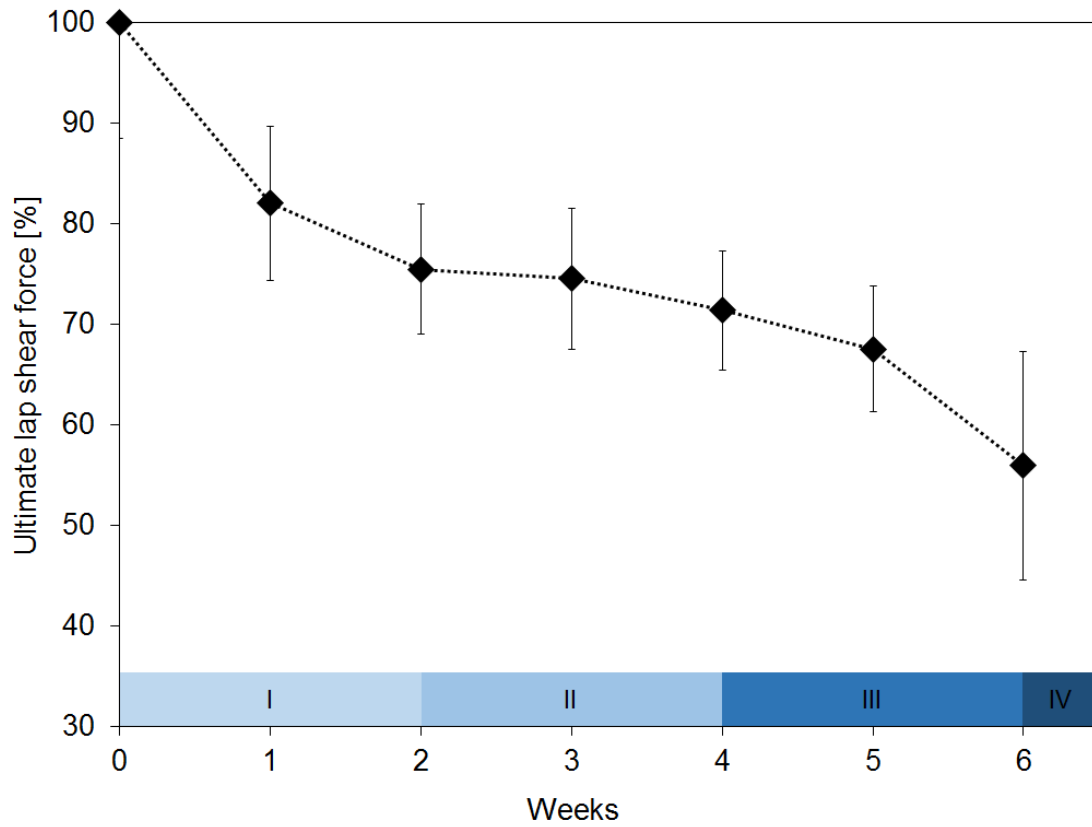


Figure 12: The residual strength of friction spot joints after the salt spray. Stage I: PPS water absorption and protection by AZ. Stage II: Transposition of AZ. Stage III: Corrosion inside PDZ. Stage IV: Final degradation of the joint.

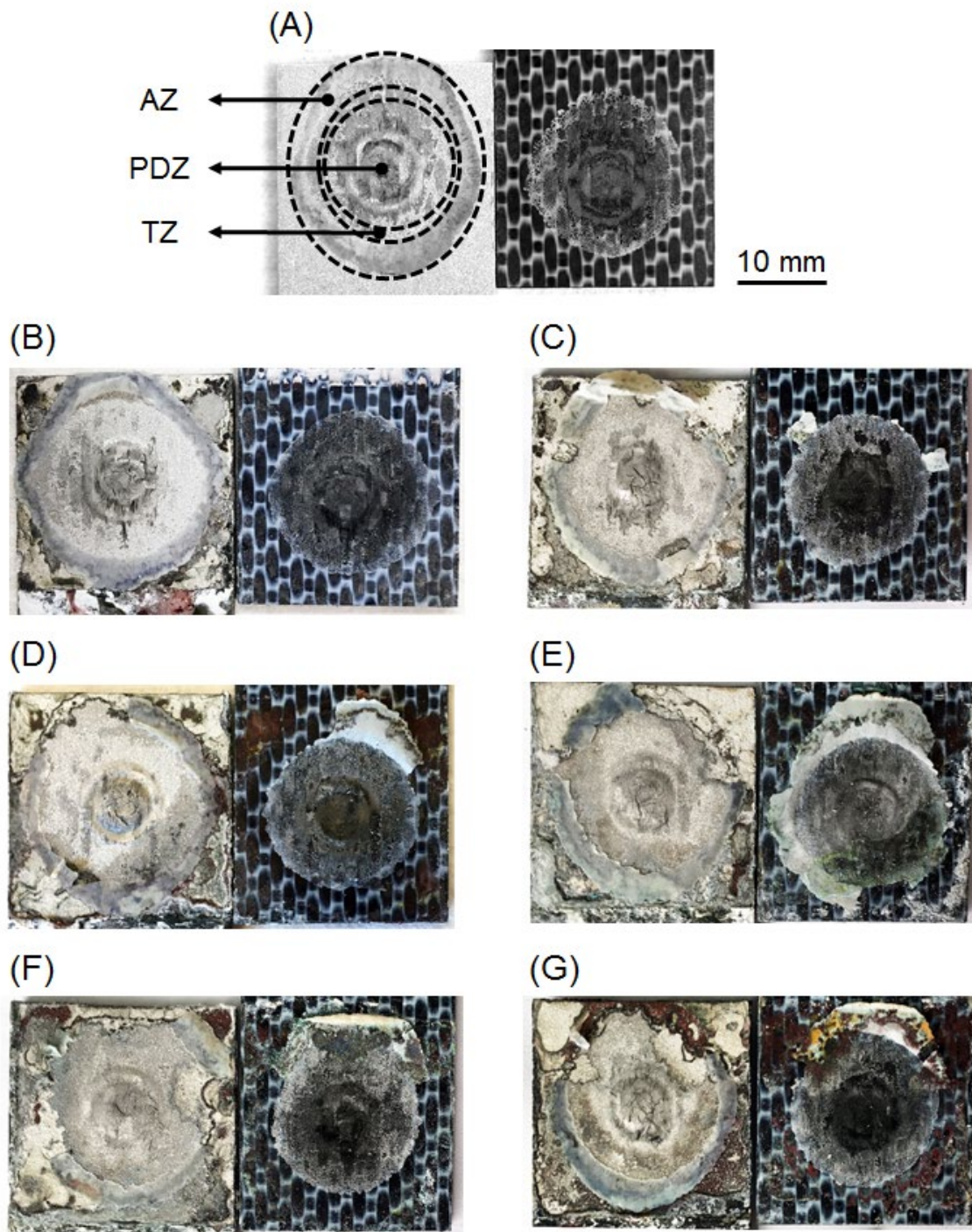


Figure 13: (A) Typical fracture surface of friction spot joints without exposure, the bonding zones are delimited by the dashed ellipses. Fracture surfaces after (B) one week, (C) two weeks, (D) three weeks, (E) four weeks, (F) five weeks, and (G) six weeks of the salt spray exposure.

Stage I comprised the first two weeks of exposure. At this early stage, a decrease of -24 % in the ultimate lap shear force (ULSF) of the joints was observed (no exposure:  $3619 \pm 132$  N; 2 weeks:  $2750 \pm$

229 N, Figure 12). The fracture surface analysis demonstrated that, at this exposure time, there was no sign of corrosion inside the bonding area of the joint. Figure 14-B shows a typical sandblasted aluminum surface close to the polymeric layer inside the PDZ. Nevertheless, the aluminum surface is severely corroded outside the bonding area as a result of self-corrosion and the galvanic coupling with CF-PPS (Figure 14-C). It is possible to note the oxide shape of the aluminum surface around the layer of the reconsolidated polymer right outside AZ (Figure 14-C). These observations demonstrate that the layer of the reconsolidated polymer in the AZ protected the core of the joint from being corroded. In this case, since no corrosion was observed inside the bonding area, the decrease in strength of the joints is attributed to the degradation of the mechanical properties of the composite part. CF-PPS can absorb water and NaCl ions. This phenomenon has been observed in several studies in the literature [45–47]. Batista *et al.* [45] observed plasticization effects in CF-PPS after the salt spray exposure due to water absorption. Decreases in  $T_g$  and increases in damping were among the main plasticization effects. The NaCl migration in the composite also reduced the stiffness of the composite due to the degradation of the fiber-matrix interface [45]. Besides the deterioration of the mechanical properties of the composite, the water absorption and NaCl intake can also induce swelling of the polymeric part, resulting in interface decoupling [48].

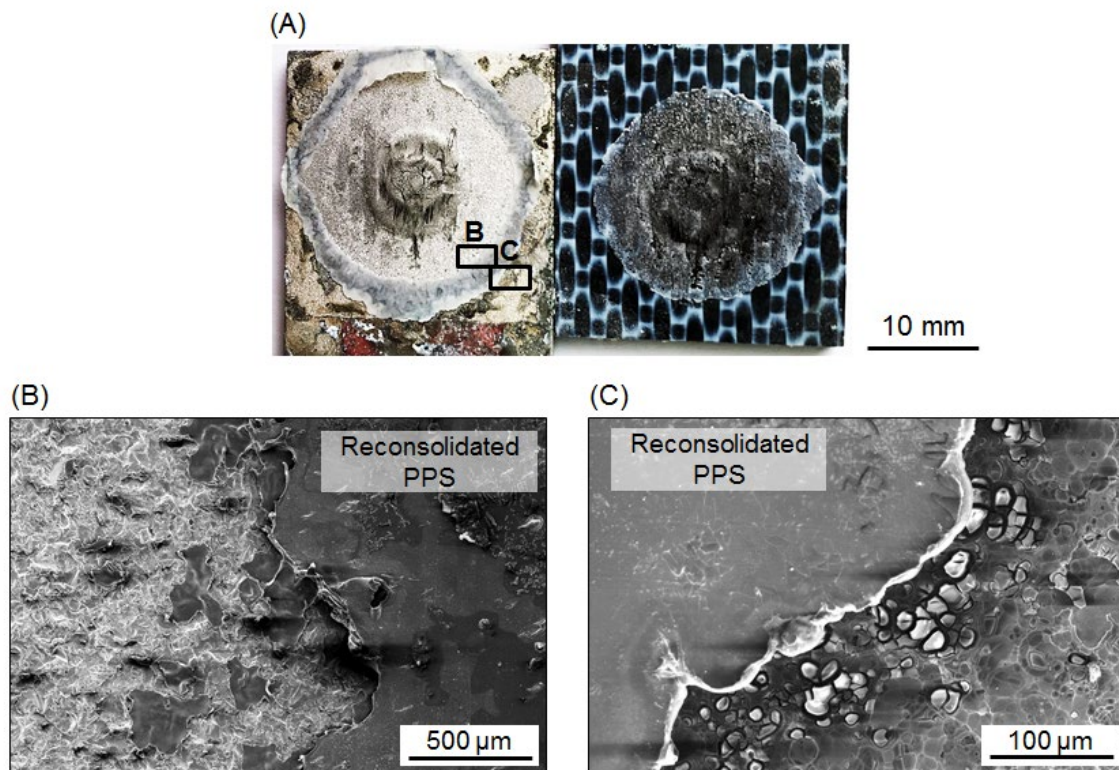


Figure 14: (A) Fracture surface of a friction spot joint after one week of salt spray exposure (Stage I). (B) Detail showing no sign of corrosion inside the PDZ. (C) Detail showing the oxidized surface of the aluminum outside the bonding zone after corrosion.

Stage II was characterized by the arresting of the strength degradation of the joints. From the second until the fourth week of exposure, the strength of the joints decreased by only 4% (Figure 12). During this stage, the reduction in strength reached -28 % ( $2605 \pm 193$  N) after four weeks of exposure. In this stage, the fracture surface analysis demonstrated that the corrosion process started to degrade the bonding area of the joints. The high temperature at the aluminum surface, combined with the pressure applied during the FSpJ process, promotes the adhesion of the molten layer of polymer and the aluminum surface [13]. Therefore, the reconsolidated polymer layer is typically strongly attached to the aluminum surface after the failure of the joints (as seen in Figure 13). However, the white arrow in Figure 15-A shows a fragment of the polymer layer that remained attached to the composite part after the failure of the joint. It indicates a weakening of the aluminum-polymer layer interface in that region as a result of the progress of the aluminum corrosion underneath the layer of polymer in the AZ. Figure 15-B exhibits signs of aluminum corrosion in the area from where the polymer layer was removed in the AZ. Nevertheless,

no corrosion morphologies were identified in the PDZ of the joints (Figure 15-C). These observations suggest that the slower strength degradation in this stage is a result of two phenomena: water and NaCl saturation of the composite, and delay of the corrosion process by the presence of the polymeric layer in the AZ. The polymer layer in the AZ acts as a barrier to be transposed by the corrosion process, since the layer of PPS functions as a protective coating well-adhered to the aluminum surface.

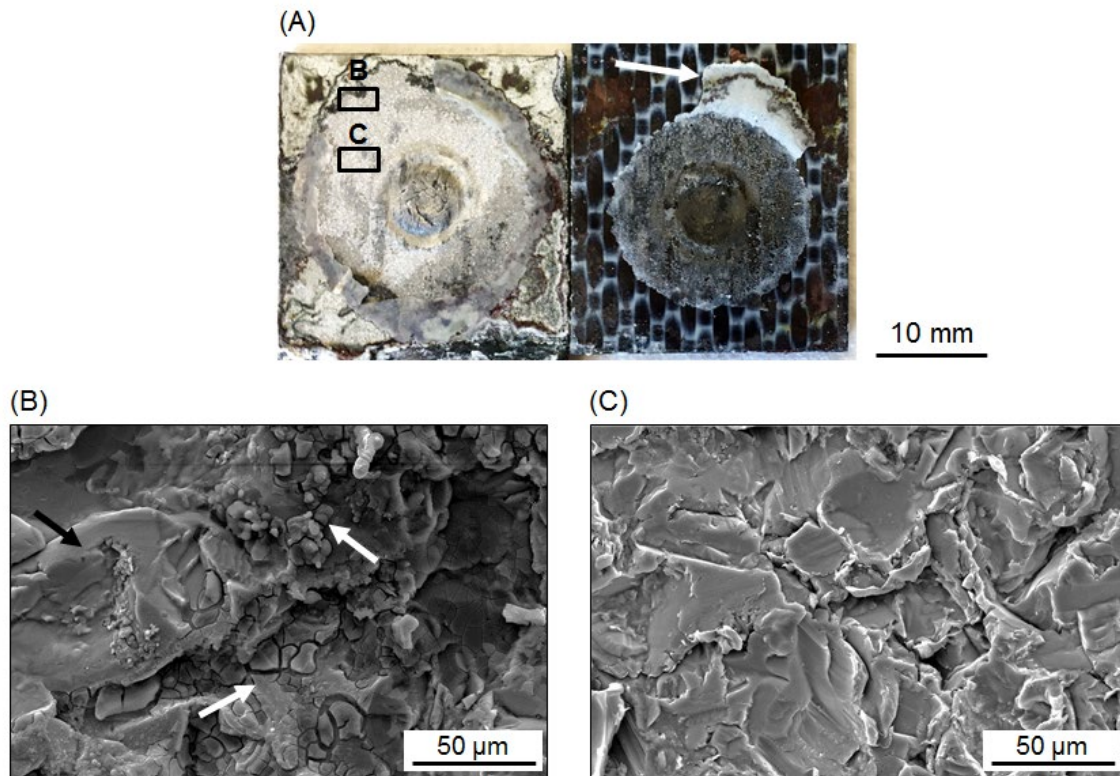


Figure 15: (A) Fracture surface of a friction spot joint after three weeks of salt spray exposure (Stage II); the white arrow indicates a fragment of the polymer layer that remained attached to the composite surface after the failure of the joint. (B) Detail showing corrosion morphologies in the area from where the polymer layer was removed at AZ. (C) Detail showing a typical sandblasted aluminum surface in the PDZ; no corroded sites.

Stage III corresponds to the final weeks of this study, the fifth and the sixth weeks. In this stage, the strength of the joints degraded rapidly, reaching a reduction of -44 % ( $2388 \pm 741$  N) of the initial ULSF after six weeks of exposure. The fracture surface analysis demonstrated that the barrier imposed by the AZ to the corrosion process was transposed in this stage. The white arrow in Figure 16-A indicates that, close to the edge of the aluminum part, the AZ is completely detached from the aluminum surface. In

this area, one observes the nuances of the corrosion process at the interface of the joints due to the presence of the polymer layer in the AZ. Figure 16-B shows the transition between the new corroded surface formed after the AZ barrier was transposed (i), and the corroded surface that was previously under the PPS layer (ii). It is noted that the corrosion process in region (ii) is more advanced than that in region (i). A flake-like surface is found in region i (Figure 16-B). This type of surface is usually found in initial stages of corrosion [49]. In contrast, region (ii) displays an oxide-like surface showing the further development of the corrosion process in this area. Additionally, Figure 17 presents the EDS analysis of regions (i) and (ii). One observes that Al and O were identified as the main elements in the corrosion product of region (i). It indicates that aluminum oxide/hydroxide is majorly formed in that region due to the corrosion process [49]. For region ii, a strong peak of Cu is observed, in addition to Al and O. The presence of Cu in the corrosion product demonstrates the de-alloying of the aluminum, indicating severer corrosion in this region [37]. These observations indicate that the presence of the polymer layer in the AZ postponed the corrosion development inside the PDZ. As discussed earlier, the polymer layer works as a barrier to the corrosion process by acting as a protective coating at the aluminum surface. Nevertheless, since the corrosion slowly advances underneath the polymer layer, a weak layer of oxides is formed at the aluminum-PPS layer interface. Consequently, the polymeric layer detaches from the aluminum surface and the corrosion advances freely to the PDZ.

Thus, corrosion sites were identified inside PDZ after six weeks of exposure (Figures 16-D and E). One observes that such regions present flake-like surface, indicating an early stage of corrosion [49]. Besides, the corrosion does not widely spread in the PDZ. It is possible to observe non-corroded areas in Figure 16-E. Therefore, it is believed that Stage IV would comprise the generalized corrosion in the PDZ, leading to the presumptive final degradation of the strength of the joints.

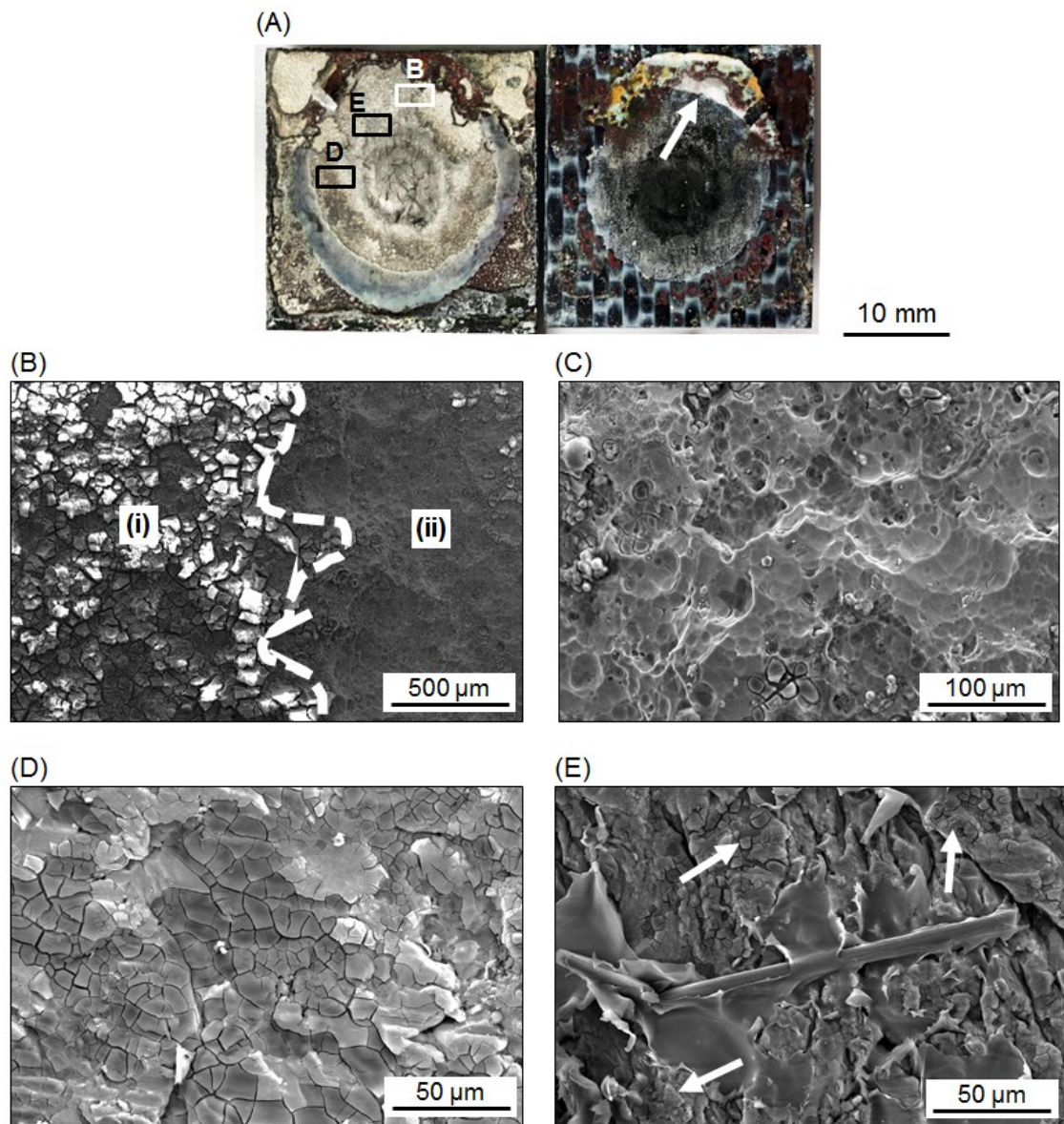


Figure 16: (A) Fracture surface of a friction spot joint after six weeks of salt spray exposure (Stage III); the white arrow indicates a fragment of the polymer layer that remained attached to the composite surface after the failure of the joint. (B) Detail showing different corroded areas due to the presence of the PPS layer at AZ. (C) Detail showing Region ii from Figure 16-B. (D) and (E) the white arrows show initial stages of corrosion inside PDZ.

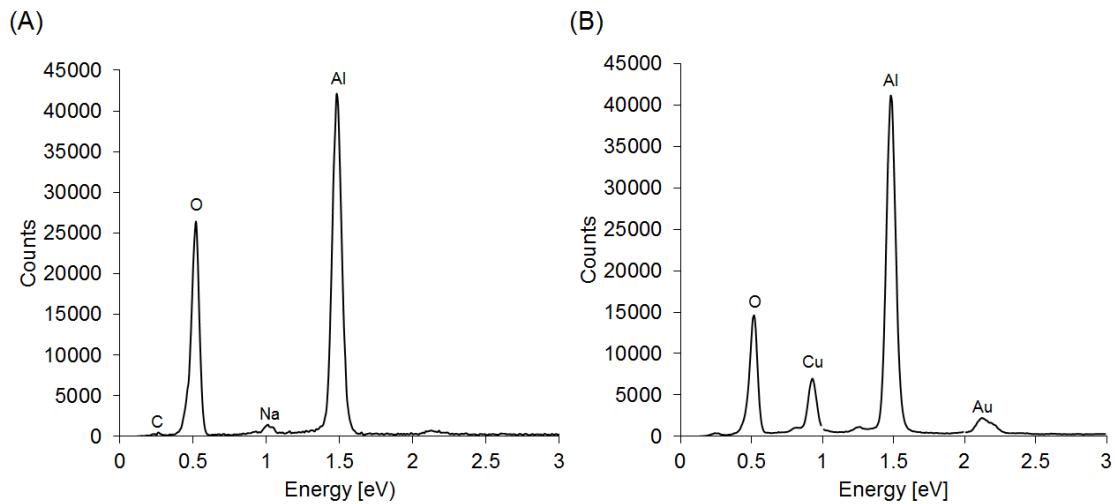


Figure 17: EDS analysis of the aluminum surface in (A) Region i and (B) Region ii from Figure 16-B.

It is worth noting that no sign of corrosive damage was found on the composite surface at any stage. This observation is as expected, given the higher anodic activity of AA2024-T3 in comparison with CF-PPS, as previously discussed in Section 3.2.1 (Figure 11).

#### 4. Conclusions

The corrosion behavior of metal–composite friction spot joints was investigated using salt spray exposure. Regarding the top surface of the joints, the aluminum part corroded preferentially in the HAZ. It was demonstrated that BM and SZ displayed a similar profile of particles, presenting a lower volume fraction of S'(S) phase than the HAZ. The higher fraction of S'(S) and coarse intermetallic particles in the HAZ increased the anodic activity in this zone. The coarse intermetallic particles lead to pitting corrosion (high self-corrosion potential), while the S'(S) precipitates are associated with intergranular corrosion (formation of precipitate-free and Cu-depletion zones around the grain boundaries). The macro-galvanic coupling between the BM, HAZ, and SZ may also potentialize the corrosion in the HAZ.

In addition, the corrosion development at the interface of the joints was evaluated. Four stages were identified and correlated with the global strength degradation of the joints:

- Stage I: Fast strength degradation of the joints (0% to -24% of ULSF). No corrosion was observed in the bonding area of the joints. Water absorption and NaCl migration into the composite caused plasticization and consequent deterioration of its mechanical properties.

- Stage II: slow strength degradation of the joints (-24% to -28% of ULSF). The slower strength degradation in this stage is a result of two phenomena: Water and NaCl saturation of the composite, and protection of the PDZ by the presence of the PPS layer in the AZ. The polymer layer acted as a protective coating well-adhered at the aluminum surface.
- Stage III: Fast strength degradation of the joints (-28% to -44% of ULSF). The development of corrosion underneath the PPS layer created a weak layer of oxides at the aluminum-PPS layer interface. Consequently, the polymeric layer detached from the aluminum surface and the corrosion advanced into the PDZ.
- Stage IV: Generalized corrosion in the PDZ and the final strength degradation of the joint.

### **Acknowledgments**

This work was supported by the Helmholtz Association (Germany) and the National Council for Scientific and Technological Development (Brazil, Process 200694/2015-4). S.T. Amancio-Filho would like to acknowledge “The Austrian aviation programme TAKE OFF” and “BMVIT-Austrian Ministry for Transport, Innovation and Technology” for the financial support.

### **References**

- [1] Faivre V, Morteau E. Airbus Tech Mag (FAST). Damage Tolerant Composite Fuselage Sizing, Characterization of Accidental Damage Threat 2011;48:10–6.
- [2] Mallick PK. Materials, design and manufacturing for lightweight vehicles. 1st ed. Cambridge, UK: Woodhead Publishing Limited; 2010.
- [3] [www.boeing.com/commercial/aeromagazine/articles/qtr\\_4\\_06/article\\_04\\_2.html](http://www.boeing.com/commercial/aeromagazine/articles/qtr_4_06/article_04_2.html) n.d.
- [4] BMW i3, the inside story: what it’s made of, how it’s made - SAE International n.d. <http://articles.sae.org/12056/> (accessed June 17, 2014).
- [5] Messler RW. Joining of Materials and Structures: From Pragmatic Process to Enabling Technology. 1 edition. Butterworth-Heinemann; 2000.
- [6] Amancio-Filho S t., dos Santos J f. Joining of polymers and polymer–metal hybrid structures: Recent developments and trends. Polym Eng Sci 2009;49:1461–76. doi:10.1002/pen.21424.
- [7] Marinelli JM, Lambing CLT. Advancement in Welding Technology for Composite-to-Metallic Joints. Journal of Advanced Materials 1994;25:20–7.

- [8] Balle F, Emrich S, Wagner G, Eifler D, Brodyanski A, Kopnarski M. Improvement of Ultrasonically Welded Aluminum/Carbon Fiber Reinforced Polymer-Joints by Surface Technology and High Resolution Analysis. *Adv Eng Mater* 2013;15:814–20. doi:10.1002/adem.201200282.
- [9] Katayama S, Kawahito Y. Laser direct joining of metal and plastic. *Scripta Materialia* 2008;59:1247–50. doi:10.1016/j.scriptamat.2008.08.026.
- [10] Mitschang P, Velthuis R, Didi M. Induction Spot Welding of Metal/CFRPC Hybrid Joints. *Advanced Engineering Materials* 2013;15:804–13.
- [11] Amancio-Filho ST, dos Santos J. European Patent EP2329905B1, 2012.
- [12] Amancio-Filho ST, Bueno C, dos Santos JF, Huber N, Hage Jr. E. On the feasibility of friction spot joining in magnesium/fiber-reinforced polymer composite hybrid structures. *Materials Science and Engineering: A* 2011;528:3841–8. doi:10.1016/j.msea.2011.01.085.
- [13] Goushegir SM, dos Santos JF, Amancio-Filho ST. Friction Spot Joining of Aluminum AA2024 / Carbon-Fiber Reinforced Poly(phenylene sulfide) composite single lap joints: microstructure and mechanical performance. *Materials & Design* 2014;50:196–206. doi:10.1016/j.matdes.2013.08.034.
- [14] Goushegir SM. Friction spot joining (FSpJ) of aluminum-CFRP hybrid structures. *Weld World* 2016;60:1073–93. doi:10.1007/s40194-016-0368-y.
- [15] André NM, Goushegir SM, dos Santos JF, Canto LB, Amancio-Filho ST. Friction Spot Joining of aluminum alloy 2024-T3 and carbon-fiber-reinforced poly(phenylene sulfide) laminate with additional PPS film interlayer: Microstructure, mechanical strength and failure mechanisms. *Composites Part B: Engineering* 2016;94:197–208. doi:10.1016/j.compositesb.2016.03.011.
- [16] Esteves JV, Goushegir SM, dos Santos JF, Canto LB, Hage Jr. E, Amancio-Filho ST. Friction spot joining of aluminum AA6181-T4 and carbon fiber-reinforced poly(phenylene sulfide): Effects of process parameters on the microstructure and mechanical strength. *Materials & Design* 2015;66:437–45. doi:10.1016/j.matdes.2014.06.070.
- [17] Jamasri, Ilman MN, Soekrisno R, Triyono. Corrosion Fatigue Behavior of Resistance Spot Welded Dissimilar Metal Welds between Carbon Steel and Austenitic Stainless Steel with Different Thickness. *Procedia Engineering* 2011;10:649–54. doi:10.1016/j.proeng.2011.04.108.
- [18] Francis R. Galvanic corrosion: a practical guide for engineers. NACE International; 2001.

- [19] Mandel M, Krüger L. Long-term Corrosion Studies of a CFRP/EN AW-6060-T6 Self-piercing rivet Joint and a Steel/EN AW-6060-T6 Blind Rivet Joint. *Materials Today: Proceedings* 2015;2:S131–40. doi:10.1016/j.matpr.2015.05.030.
- [20] L. F. M. da Silva (editor). *Hybrid Adhesive Joints*. Springer, 2011. n.d.
- [21] Bellucci F, Martino AD, Liberti C. Electrochemical behaviour of graphite-epoxy composite materials (GECM) in aqueous salt solutions. *J Appl Electrochem* 1986;16:15–22. doi:10.1007/BF01015979.
- [22] American Society for Testing and Materials. Philadelphia, editor. *Standard guide for development and use of a galvanic series for predicting galvanic corrosion performance*. West Conshohocken, PA: ASTM; 1998.
- [23] Degarmo PE, Black JT, Kohser RA. *Materials and Processes in Manufacturing*. Wiley; 2003.
- [24] American Society for Metals, American Society for Metals. *Metals Handbook*. Volume 2, Volume 2,. Metals Park, Ohio: American Society for Metals; 1981.
- [25] GHOSH KS, HILAL M, BOSE S. Corrosion behavior of 2024 Al-Cu-Mg alloy of various tempers. *Transactions of Nonferrous Metals Society of China* 2013;23:3215–27. doi:10.1016/S1003-6326(13)62856-3.
- [26] Fiore V, Calabrese L, Proverbio E, Passari R, Valenza A. Salt spray fog ageing of hybrid composite/metal rivet joints for automotive applications. *Composites Part B: Engineering* 2017;108:65–74. doi:10.1016/j.compositesb.2016.09.096.
- [27] Pan Y, Wu G, Cheng X, Zhang Z, Li M, Ji S, et al. Galvanic corrosion behaviour of carbon fibre reinforced polymer/magnesium alloys coupling. *Corrosion Science* 2015;98:672–7. doi:10.1016/j.corsci.2015.06.024.
- [28] Davis JR. *Aluminum and Aluminum Alloys*. Materials Park, OH: ASM International; 1993.
- [29] Aluminium AA2024-T3 technical datasheet. Constellium France; 2012. n.d.
- [30] Tencate Advanced Composites. CETEX® PPS Technical Datasheets, Tencate Advanced Composites 2009.
- [31] André NM, Goushegir SM, Scharnagl N, Santos JF dos, Canto LB, Amancio-Filho ST. Composite surface pre-treatments: Improvement on adhesion mechanisms and mechanical performance

of metal–composite friction spot joints with additional film interlayer. *The Journal of Adhesion* 2017;0:1–20. doi:10.1080/00218464.2017.1378101.

[32] Goushegir SM, dos Santos JF, Amancio-Filho ST. Influence of aluminum surface pre-treatments on the bonding mechanisms and mechanical performance of metal-composite single-lap joints. *Weld World* 2017;61:1099–115. doi:10.1007/s40194-017-0509-y.

[33] Hammersley AP, Svensson SO, Hanfland M, Fitch AN, Hausermann D. Two-dimensional detector software: From real detector to idealised image or two-theta scan. *High Pressure Research* 1996;14:235–48. doi:10.1080/08957959608201408.

[34] Pedersen JS. Determination of size distribution from small-angle scattering data for systems with effective hard-sphere interactions. *J Appl Cryst, J Appl Crystallogr* 1994;27:595–608. doi:10.1107/S0021889893013810.

[35] Genevois C, Deschamps A, Denquin A, Doisneau-cottignies B. Quantitative investigation of precipitation and mechanical behaviour for AA2024 friction stir welds. *Acta Materialia* 2005;53:2447–58. doi:10.1016/j.actamat.2005.02.007.

[36] CHEN Y, DING H, LI J, ZHAO J, FU M, LI X. Effect of welding heat input and post-welded heat treatment on hardness of stir zone for friction stir-welded 2024-T3 aluminum alloy. *Transactions of Nonferrous Metals Society of China* 2015;25:2524–32. doi:10.1016/S1003-6326(15)63871-7.

[37] Glenn AM, Muster TH, Luo C, Zhou X, Thompson GE, Boag A, et al. Corrosion of AA2024-T3 Part III: Propagation. *Corrosion Science* 2011;53:40–50. doi:10.1016/j.corsci.2010.09.035.

[38] Zhang X, Zhou X, Hashimoto T, Liu B. Localized corrosion in AA2024-T351 aluminium alloy: Transition from intergranular corrosion to crystallographic pitting. *Materials Characterization* 2017;130:230–6. doi:10.1016/j.matchar.2017.06.022.

[39] Zhou X, Luo C, Hashimoto T, Hughes AE, Thompson GE. Study of localized corrosion in AA2024 aluminium alloy using electron tomography. *Corrosion Science* 2012;58:299–306. doi:10.1016/j.corsci.2012.02.001.

[40] Kang J, Fu R, Luan G, Dong C, He M. In-situ investigation on the pitting corrosion behavior of friction stir welded joint of AA2024-T3 aluminium alloy. *Corrosion Science* 2010;52:620–6. doi:10.1016/j.corsci.2009.10.027.

- [41] Seetharaman R, Ravisankar V, Balasubramanian V. Corrosion performance of friction stir welded AA2024 aluminium alloy under salt fog conditions. *Trans Nonferrous Met Soc China* 2015;25:1427–38. doi:10.1016/S1003-6326(15)63742-6.
- [42] Jariyaboon M, Davenport AJ, Ambat R, Connolly BJ, Williams SW, Price DA. The effect of welding parameters on the corrosion behaviour of friction stir welded AA2024–T351. *Corrosion Science* 2007;49:877–909. doi:10.1016/j.corsci.2006.05.038.
- [43] Yasakau KA, Zheludkevich ML, Lamaka SV, Ferreira MGS. Mechanism of Corrosion Inhibition of AA2024 by Rare-Earth Compounds. *J Phys Chem B* 2006;110:5515–28. doi:10.1021/jp0560664.
- [44] Bousquet E, Poulon-Quintin A, Puiggali M, Devos O, Touzet M. Relationship between microstructure, microhardness and corrosion sensitivity of an AA 2024-T3 friction stir welded joint. *Corrosion Science* 2011;53:3026–34. doi:10.1016/j.corsci.2011.05.049.
- [45] Batista NL, Rezende MC, Botelho EC. Effect of crystallinity on CF/PPS performance under weather exposure: Moisture, salt fog and UV radiation. *Polymer Degradation and Stability* 2018;153:255–61. doi:10.1016/j.polyimdegradstab.2018.03.008.
- [46] Lopes de Oliveira MC, Sayegh IJ, Ett G, Antunes RA. Corrosion behavior of polyphenylene sulfide–carbon black–graphite composites for bipolar plates of polymer electrolyte membrane fuel cells. *International Journal of Hydrogen Energy* 2014;39:16405–18. doi:10.1016/j.ijhydene.2014.07.175.
- [47] Gellert EP, Turley DM. Seawater immersion ageing of glass-fibre reinforced polymer laminates for marine applications. *Composites Part A: Applied Science and Manufacturing* 1999;30:1259–65. doi:10.1016/S1359-835X(99)00037-8.
- [48] Arhant M, Le Gac P-Y, Le Gall M, Burtin C, Briançon C, Davies P. Effect of sea water and humidity on the tensile and compressive properties of carbon-polyamide 6 laminates. *Composites Part A: Applied Science and Manufacturing* 2016;91:250–61. doi:10.1016/j.compositesa.2016.10.012.
- [49] Hughes AE, Boag A, Glenn AM, McCulloch D, Muster TH, Ryan C, et al. Corrosion of AA2024-T3 Part II: Co-operative corrosion. *Corrosion Science* 2011;53:27–39. doi:10.1016/j.corsci.2010.09.030.